# Embedded Finite-Element Solver for Computation of Brushless Permanent-Magnet Motors

T. J. E. Miller, *Fellow, IEEE*, Mircea Popescu, *Senior Member, IEEE*, Calum Cossar, Malcolm I. McGilp, Mircea Olaru, Alan Davies, Jonathan Sturgess, and Alessandra Sitzia, *Member, IEEE*

***Abstract*—This paper describes the theory underlying the formulation of a "minimum set" of finite-element solutions to be used in the design and analysis of saturated brushless permanent-magnet motors. The choice of finite-element solutions is described in terms of key points on the flux–MMF diagram. When the diagram has a regular shape, a huge reduction in finite-element analysis is possible with no loss of accuracy. If the loop is irregular, many more solutions are needed. This paper describes an efficient technique in which a finite-element solver is associated with a classical $d$–$q$-axis circuit model in such a way that the number of finite-element solutions in one electrical half-cycle can be varied between 1 and 360. The finite-element process is used to determine not only the average torque but also the saturated inductances as the rotor rotates.**

***Index Terms*—Brushless permanent-magnet (PM) motors, finite-element method, simulation, torque calculation.**

## NOMENCLATURE

| | |
|---|---|
| $i$ | Instantaneous current (in amperes). |
| $m$ | Number of phases. |
| $v$ | Instantaneous voltage (in volts). |
| $p$ | Operator $d/dt$; or number of pole pairs. |
| $\psi$ | Instantaneous flux linkage (in volt seconds). |
| $\theta$ | Rotor angular position (in radians). |
| $R$ | Phase resistance (in ohms). |
| $T$ | Electromagnetic torque (in newton meters). |
| $W$ | Energy conversion loop area per phase (in joules). |
| $\gamma$ | Phase-advance angle of the current relative to EMF (in electrical degrees). |
| $\omega$ | Speed (in electrical radians per second). |
| $d, q$ | (Subscripts) Direct and quadrature axes, respectively. |

Paper IPCSD-07-110, presented at the 2006 Industry Applications Society Annual Meeting, Tampa, FL, October 8–12, and approved for publication in the IEEE TRANSACTIONS ON INDUSTRY APPLICATIONS by the Electric Machines Committee of the IEEE Industry Applications Society. Manuscript submitted for review October 29, 2006 and released for publication November 10, 2007. Published July 23, 2008 (projected).

T. J. E. Miller, M. Popescu, C. Cossar, and M. I. McGilp are with the SPEED Laboratory, Department of Electronics and Electrical Engineering, University of Glasgow, Glasgow, G12 8LT, U.K. (e-mail: t.miller@elec.gla.ac.uk; mircea@elec.gla.ac.uk; calum@elec.gla.ac.uk; mal@elec.gla.ac.uk; www.speedlab.co.uk).

M. Olaru is with ICNDMF-CEFIN, 70314 Bucharest, Romania (e-mail: mirceaolaru2@yahoo.com).

A. Davies, J. Sturgess, and A. Sitzia are with the AREVA T&D Technology Centre, Stafford, ST17 4LN, U.K. (e-mail: alan.davies@areva-td.com; jonathan.sturgess@areva-td.com; alessandra.sitzia@areva-td.com; www.areva-td.com).

Color versions of one or more of the figures in this paper are available online at http://ieeexplore.ieee.org.

Digital Object Identifier 10.1109/TIA.2008.926199

## I. INTRODUCTION

BRUSHLESS permanent-magnet (PM) motors are widely used in a range of applications including electric and hybrid vehicles, servo motors, high-efficiency pumping applications, and many others, whereas new applications are emerging as a result of the high efficiency, low noise, and controllability of these machines [1], [2], [5]. Both sinewave and squarewave drives are used, with a huge range of motor geometries, winding configurations, and materials. In many cases, the motor is driven to extremes of saturation and/or very high speed, so that the waveforms of current and terminal voltage are often nonsinusoidal. Even when ideal sinusoidal conditions prevail, the parameters may vary widely from the no-load values.

The circuit and control conditions often cover a wide range of operating points. For simulation purposes, a classical equivalent circuit model of the machine is required, based on conventional theory, even though the saturable parameters (inductances and flux linkages) must be computed by the finite-element method, for the sake of accuracy. The challenge is to make accurate performance simulations with the minimum "overhead" of finite-element calculation. Preferably also, the circuit parameters should be made available in a form which shows their dependence on current and even rotor position, so that lookup tables or interpolating functions can be used in simulation and control.

It is shown in this paper that the flux–MMF diagram or "$i-\psi$ loop" provides a completely general method for computation of any synchronous machine, in which the key outputs are the average electromagnetic torque and the saturated inductances averaged over one cycle. "Completely general" means that the method works equally well with any rotor geometry, any winding distribution, and any current waveform. Moreover, the shape of the $i-\psi$ loop itself directly indicates whether it will be possible to use a "reduced-order" model of the machine, such as the $d$–$q$-axis model with fixed parameter values. When the $i-\psi$ loop is elliptical, the ellipse has several special properties which are useful in design and simulation, which are brought out in this paper.

In this special case, an accurate value of the average torque can be obtained with only a single finite-element computation. Moreover, the synchronous inductances in this case are independent of rotor position, even though they may be heavily saturated.

In all other cases, when the $i-\psi$ loop is not elliptical, the number of finite-element computations required for accurate torque calculation is greater than one, and the number required

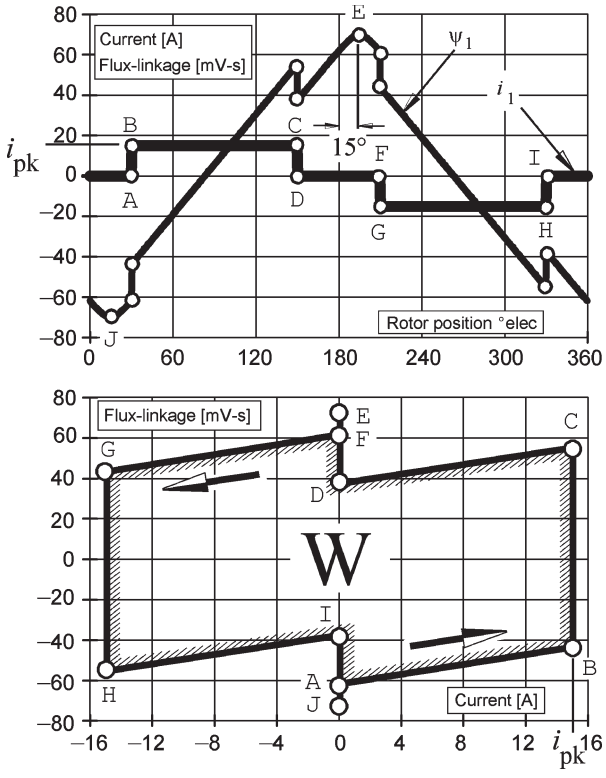


Fig. 1. Current and flux-linkage waveforms and $i-\psi$ loop: Squarewave drive.

depends on the regularity of the diagram: In particular, the number of solutions depends on the number of points on the boundary of the loop, which are necessary to define its area precisely.

An important feature of this paper is that the finite-element method is used only for magnetostatic calculations. In other words, the differential circuit equations (terminal voltage equations) should be solved with a circuit simulator, whereas the finite-element analysis remains magnetostatic and current driven. Although it is possible to solve the differential voltage equations by incorporating them in the schema of a finite-element program, such a solution will be slow and difficult to relate to a theoretical model of the control [10].

## II. Theory

### A. Three-Phase Brushless PM Motor With Squarewave Drive

Fig. 1 shows the current and flux-linkage waveforms in one phase of a three-phase brushless PM motor with squarewave drive, operating at low speed when the current can be accurately regulated to follow the ideal 120E rectangular waveform. The current waveform is phase advanced by 15E relative to the flux-linkage waveform. The phase EMF (not shown) is the derivative of the flux-linkage $d\psi/dt$, and the $i-\psi$ diagram is shown at the bottom. This diagram is simply the "$x-y$ plot" or Lissajous figure obtained by plotting $\psi$ versus $i$. The average electromagnetic torque $T$ is given by

$$T = mp\frac{W}{2\pi}. \tag{1}$$

The $i-\psi$ loop has a remarkably regular shape, such that the area $W$ can be estimated as twice the area of parallelogram ABCD [2], and

$$W = 2i_{\rm pk}(\psi_{\rm C} - \psi_{\rm B}). \tag{2}$$

It appears that only two electromagnetic field evaluations are required (at B and C) to determine this area. If the phase-advance angle is zero, the offset between the two parallelograms ABCD and FGHI disappears, such that $\rm D = F$ and $\rm A = I$, and in this case, only one field evaluation is required (because $\psi_{\rm B} = -\psi_{\rm C}$). If the field evaluations are to be done by the finite-element method, the $i-\psi$ loop diagram indicates which finite-element solutions are required, and it gives a very good indication of how many solutions are required. No such guidance is available in the time waveforms in the upper part of Fig. 1. In terms of these waveforms, the average electromagnetic torque can be expressed as

$$T = \frac{mp}{2\pi}\int_0^{2\pi}\psi\frac{\partial i}{\partial\theta}d\theta \tag{3}$$

which is equivalent to (1) but is more difficult to evaluate because it does not take advantage of the simplicity of the shape of the loop or any of its particular features. It also requires many more evaluations of $\psi$ and $i$.

### B. Other Useful Deductions From the $i-\psi$ Loop

In Fig. 1, neither the current nor the flux linkage is sinusoidal. Therefore, phasors cannot be used, even though both quantities are "alternating." The effect of "armature reaction," i.e., the additional flux linkage due to the current, can be seen in Fig. 1 as a kind of dislocated segment of the flux-linkage waveform in each half-cycle.

The effect of armature reaction is clearly not constant over the cycle. For example, at the beginning of the segment BC, the armature reaction is demagnetizing (i.e., opposing the magnet flux), whereas at the end, it is magnetizing. This means that the leading edge of the magnet is subject to demagnetization, whereas the trailing edge is subject to remagnetization, as the rotor passes the axis of the phase winding.

In the example shown in Fig. 1, the peak flux linkage occurs at E in the positive sense and at J in the negative sense. The peak occurs during an interval when the corresponding phase current is zero. However, this is not an open-circuit condition because the current is flowing through phases 2 and 3 during this interval. For the magnet pole in question, the armature reaction is then largely cross-magnetizing. In heavily saturated motors, this cross-magnetization can influence the apparent "open-circuit" flux at points E and J.

In the example in Fig. 1, the peak flux linkage does not coincide with the peak current, but the current could be increased to a level such that $\psi_{\rm C} > \psi_{\rm E}$. It thus appears that peak flux densities will be associated with points E or C, and it would be reasonable to use these points as "test points" for finite-element analysis to determine these flux densities.

TABLE I
FINITE-ELEMENT SOLUTIONS REQUIRED FOR SQUAREWAVE DRIVE

| | |
|---|---|
| Peak flux-densities | C, E |
| Maximum demagnetization | B |
| Average torque | B,C |
| Phase inductance | C,D |
| Short-circuit current | E,C,D |
| Open-circuit EMF | E |

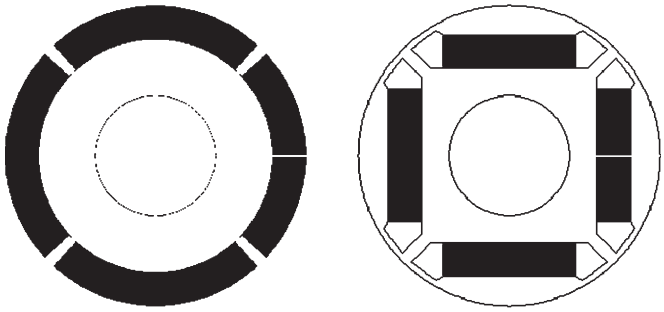

Fig. 2. (Left) Surface-magnet and (right) interior-magnet rotors.

Likewise, it appears that the maximum demagnetization will occur at points B and G, and again, one of these points could be used as a test point for finite-element analysis.

The phase inductance is also equal to the slope of the line DC, and the short-circuit current is equal to $\psi_{\mathrm{E}}$ divided by this inductance. The average open-circuit EMF is given by $\psi_{\mathrm{E}}/\pi$ multiplied by the speed in electrical radians per second.

These interpretations can be summarized in the form of a table indicating the most useful finite-element computation problems to solve during the design phase, as shown in Table I.

With any programmable finite-element software, it therefore makes sense to prepare a "GoFER"—an automatic process that "Goes to Finite-Elements and Returns" a useful set of results—for a predetermined sequence of points on the $i-\psi$ diagram. For squarewave motors, as discussed earlier, the most useful points in the GoFER would be B, C, D, and E.

A simple GoFER comprising only four points is adequate for surface-magnet motors operating with squarewave drive current waveforms, when the level of saturation is low. Finite-element analysis is still desirable, even in these apparently simple cases, because the geometrical detail is often difficult to calculate accurately by classical methods such as the magnetic equivalent circuit method. Indeed, the geometric complexity is not the only reason: The winding configuration may also be complex and not amenable to the computation of flux linkage and EMF by traditional methods. In the case of axial-flux machines where 3-D finite-element analysis is required, the computational efficiency of the GoFER process is even more valuable.

### C. Three-Phase Brushless PM Motor With Sinewave Drive

While the surface-magnet rotor (Fig. 2) can be used with either squarewave or sinewave drive, the interior-magnet rotor is better adapted to sinewave drive because of its saliency and its strongly nonlinear characteristics. With sinewave drive, the current waveform is ideally sinusoidal, and ideally, the flux-linkage waveform in each phase is also sinusoidal. Under these conditions, current, flux linkage, and EMF can all be represented as phasors, and the $i-\psi$ loop is a pure ellipse, as shown in Fig. 3.

In many cases, the steady-state performance of a motor with sinewave drive can be computed using values of the synchronous inductances $L_d$ and $L_q$, and of the magnet flux linkage $\Psi_{Md1}$, which are strongly affected by saturation but which remain independent of rotor position. Indeed, many of the published analyses of saturated brushless PM and synchronous reluctance motors are based on this precept. There are many documented cases of interior-magnet motors in which $L_q$ can vary by as much as 5 : 1 between no load and full load, whereas the $q$-axis flux can saturate the pole pieces and the stator teeth to such an extent that the effective magnet flux linkage $\Psi_{Md1}$ is also affected.

Such cases are ideally characterized by constant values of $i_d$, $i_q$, $\psi_d$, and $\psi_q$ throughout the electrical cycle, consistent with the elliptical energy-conversion loop in each phase (see Fig. 3). If $L_d$, $L_q$, and the magnet flux linkage $\Psi_{Md1}$ also remain constant throughout the cycle, it suffices to calculate these parameters at only one instant during the cycle.

The objective is to determine suitable "saturated" values of $L_d$, $L_q$, and $\Psi_{Md1}$ to be used in the flux-linkage equations

$$\psi_d = \Psi_{Md1} + L_d i_d \tag{4a}$$

$$\psi_q = L_q i_q. \tag{4b}$$

$L_d$ and $L_q$ are both affected by saturation, with $L_q$ being mainly a function of $i_q$ and with $L_d$ being mainly a function of $i_d$. To some extent, $L_d$ is a function of $i_q$, and $L_q$ is a function of $i_d$, because of "cross-saturation." $\Psi_{Md1}$ is also affected by saturation, notably by the saturation caused by $i_q$ when $i_d = 0$.

For any set of values of $i_d$ and $i_q$, the flux linkages $\psi_d$ and $\psi_q$ can be computed by finite-element analysis, and then, $L_d$ and $L_q$ can be deduced from (4a) and (4b) as

$$L_d = \frac{\psi_d - \Psi_{Md1}}{i_d} \tag{5a}$$

$$L_q = \frac{\psi_q}{i_q}. \tag{5b}$$

A unique value of $L_q$ can be deduced from (5b), with $i_q$ being equal to the value defined by the load point. However, in order to deduce $L_d$, we also need a value for the "open-circuit" flux linkage $\Psi_{Md1}$. The obvious choice is to set $\Psi_{Md1}$ equal to the true open-circuit value, which can be computed with $i_d = 0$ and $i_q = 0$. However, (4) suggests an alternative in which $\Psi_{Md1}$ is computed with $i_d = 0$, whereas $i_q$ retains the load-point value as used in (5b). In this case, $\Psi_{Md1}$ is computed with the full effect of cross-saturation in the $q$-axis, which tends to decrease its value. Thereafter, the additional term $L_d i_d$ can be interpreted as the flux linkage of armature reaction in the $d$-axis, in the presence of the cross-magnetizing current $i_q$.

This interpretation is "heuristic," and not mathematically rigorous, because it tacitly relies on the notion of superposition. However, the process is systematic and reproducible and makes

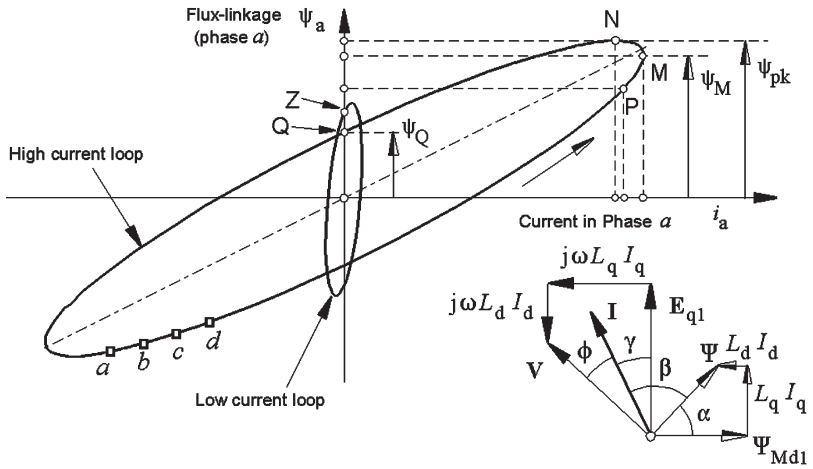


Fig. 3. Elliptical $i-\psi$ diagram with sinusoidal current and flux linkage.

sense in engineering terms because it somehow separates the effect of $L_d$ and $i_d$ from the effect of $i_q$. It also avoids the need to account for cross-saturation by introducing an artificial mutual inductance $L_{dq}$ with an additional term in (4a) and (4b). This term would itself be saturable. There is, in fact, an infinite number of possible values of $\Psi_{Md1}$ and $L_d$ that will satisfy (4a). The reason is that the superposition implied by the addition in this equation is not valid under saturated conditions.

If $\Psi_{Md1}$ is evaluated with $i_d = 0$ and $i_q = 0$, there is a possibility for the numerator $(\psi_d - \Psi_{Md1})$ to become nonzero when $i_q$ is restored to the normal load-point value, even when $i_d = 0$. Equation (5a) would then produce an indefinite result for $L_d$ if it was used at (or near) such a load point where $i_d = 0$ and where $i_q$ was nonzero, which is quite a normal condition. This problem is avoided if, as suggested, $\Psi_{Md1}$ is calculated with $i_d = 0$ and the load-point value of $i_q$.

### *D. Properties of the Elliptical Energy-Conversion Loop ($i-\psi$ Diagram)*

Two elliptical $i-\psi$ loops are shown in Fig. 3 for two operating conditions: one at high current and one at low current. The general form of the phasor diagram is also shown, together with the space phasor diagram of flux linkages, in which $\mathbf{\Psi}_{Md1}$ is the notional "open-circuit" flux linkage due to the magnet. $L_dI_d$ and $L_qI_q$ are the flux linkages of armature reaction in the $d$- and $q$-axes, respectively. The rotating fluxes associated with these flux linkages generate the respective induced voltages in the phasor diagram; thus, $\mathbf{\Psi}_{Md1}$ generates $j\omega_{q1}$, $L_dI_d$ generates $j\omega L_dI_d$, $L_qI_q$ generates $j\omega L_qI_q$, and the resultant $\mathbf{\Psi}$ generates the "air-gap voltage" $\mathbf{V}$. Resistance is omitted.

For the high-current loop, the current reaches its maximum positive value at M and passes through a negative-going zero at Q. The flux linkage $\psi_a$ reaches its maximum value at N. Because the loop is traversed counterclockwise, M precedes N. This is consistent with the fact that $\mathbf{I}$ leads $\mathbf{\Psi}$.

The phasor diagram tells us that the angle of rotation between M and N is $\beta$, which is the phase angle in electrical degrees between the current phasor $\mathbf{I}$ and the flux-linkage phasor $\mathbf{\Psi}$. If we take the "open-circuit" flux linkage $\mathbf{\Psi}_{Md1}$ as reference, we can use the phasor diagram to write the following equations for the instantaneous currents, with $\theta = \omega t$:

$$\begin{aligned} i_a &= i_{\rm pk}\cos(\pi/2+\gamma+\theta) = -i_{\rm pk}\sin(\gamma+\theta) \\ i_b &= -i_{\rm pk}\sin(\gamma+\theta-2\pi/3) \\ i_b &= -i_{\rm pk}\sin(\gamma+\theta+2\pi/3). \end{aligned} \tag{6}$$

Note that $i_{\rm pk}$ is the abscissa at point M. If these equations are substituted in the forward $dq$ transformation, we get

$$I_d = -i_{\rm pk}\sin\gamma \quad I_q = +i_{\rm pk}\cos\gamma \tag{7}$$

in which $I_d$ and $I_q$ are constant. The corresponding equations for the instantaneous flux linkages are

$$\begin{aligned} \psi_a &= \psi_{\rm pk}\cos(\pi/2+\gamma-\beta+\theta) = -\psi_{\rm pk}\sin(\gamma-\beta+\theta) \\ \psi_b &= -\psi_{\rm pk}\sin(\gamma-\beta+\theta-2\pi/3) \\ \psi_b &= -\psi_{\rm pk}\sin(\gamma-\beta+\theta+2\pi/3). \end{aligned} \tag{8}$$

Note that $\psi_{\rm pk}$ is the ordinate at point N. Again, from the $dq$ transformation, we get

$$\begin{aligned} \psi_d &= -\psi_{\rm pk}\sin(\gamma-\beta) = \psi_{\rm pk}\cos\alpha \\ \psi_q &= +\psi_{\rm pk}\cos(\gamma-\beta) = \psi_{\rm pk}\sin\alpha. \end{aligned} \tag{9}$$

Like $I_d$ and $I_q$, these are constant values; they do not appear in Fig. 3.

When $i_a = 0$, we have $i_b = -(\sqrt{3}/2)i_{\rm pk}$ and $i_c = +(\sqrt{3}/2)i_{\rm pk}$, and this represents a negative-going zero of $i_a$ at the instant Q defined by $\gamma + 2 = 0$, or $\omega t = -\gamma$. The value of $\psi_a$ at this point (Q) is given by

$$\psi_a = \psi_{\rm pk}\sin\beta = \psi_{\rm Q}. \tag{10}$$

Thus, when $i_a = 0$, the flux linkage $\psi_a$ in phase $a$ at point Q is not simply the open-circuit value but depends on the inductances $L_d$ and $L_q$ and the phase angle $\beta$. In fact, the true open-circuit flux linkage is not observable in Fig. 3, unless the $i-\psi$ loop is drawn for zero current. When this is done, the loop degenerates into a vertical straight line, and the maximum value

of $\psi_a$ is equal to the peak open-circuit flux linkage $\sqrt{2}\Psi_{Md1}$. The low-current loop in Fig. 3 shows this point very nearly at Z. There is no simple relationship between Z and Q. However, note that the $\psi$ values at Q and N are in the ratio $\sin\beta$.

When $\gamma = 0$, the current is in the $q$-axis, and $\psi_{\rm Q}$ is then equal to the peak value of "magnet flux linkage" in phase $a$ because $\beta = \pi/2 - \boldsymbol{\alpha}$ and $\psi\cos\alpha = \psi\sin\beta\Psi_{Md1}$. If the magnetic circuit is linear, this is equal to the open-circuit value of the magnet flux linkage in phase $a$ because, although $i_b$ and $i_c$ are not zero at point Q, they produce a transverse flux which does not link phase $a$. In that case, points Q and Z are coincident. However, if $I_q$ is sufficient to cause appreciable saturation of the magnetic circuit, then $\sin\beta$ and $\psi_{\rm Q}$ can both be affected. In that case, point Q deviates from point Z.

Another point of interest on the ellipse diagram is M, where $i_a = i_{\rm pk}$. At this point, $\sin(\gamma+\theta) = -1$, so $\theta = \gamma + \pi/2$, and if this is substituted in (8), we get

$$\psi_a = \psi_{\rm pk}\cos\beta = \psi_{\rm M}. \tag{11}$$

Note the ratio

$$\frac{\psi_{\rm Q}}{\psi_{\rm M}} = \tan\beta. \tag{12}$$

However, $\beta$ can be written as $\pi/2 - \varphi$, where $\varphi$ is the "internal power-factor angle," i.e., the phase angle between the "internal" or "air-gap" voltage $\mathbf{V}$ and the current $\mathbf{I}$. Then,

$$\tan\varphi = \frac{\psi_{\rm M}}{\psi_{\rm Q}} \tag{13}$$

from which the internal power factor $\cos\varphi$ can easily be determined. When $\cos\beta = 0$, $\beta = \pi/2$, and the current $\mathbf{I}$ is in quadrature with the flux linkage $\psi$. In this case, M lies on the horizontal axis, and the ellipse is not tilted; the internal power factor is then one. Although this condition represents the maximum possible internal power factor, it does not necessarily indicate the maximum torque per ampere, unless $L_d = L_q$. The greater the tilt angle, the lower the internal power factor.

The average electromagnetic torque can be calculated using $d, q$ values for flux linkage and current in the well-known equation

$$T = mp(\Psi_d I_q - \Psi_q I_d). \tag{14}$$

The $d, q$ values can be determined from instantaneous values using the following:

$$\Psi_d = \frac{1}{\sqrt{2}}\psi_{\rm pk}\cos\alpha \quad \Psi_q = \frac{1}{\sqrt{2}}\psi_{\rm pk}\sin\alpha$$
$$I_d = -\frac{1}{\sqrt{2}}i_{\rm pk}\sin\gamma \quad I_q = \frac{1}{\sqrt{2}}i_{\rm pk}\cos\gamma. \tag{15}$$

Substituting in (14)

$$T = mp\frac{1}{2}\psi_{\rm pk}i_{\rm pk}(\cos\alpha\cos\gamma + \sin\alpha\sin\gamma)$$
$$= mp\frac{1}{2}\psi_{\rm pk}i_{\rm pk}\cos(\alpha-\gamma). \tag{16}$$

TABLE II
FINITE-ELEMENT SOLUTIONS REQUIRED FOR SINEWAVE DRIVE

| | |
|---|---|
| Peak flux-densities | N |
| Maximum demagnetization | M |
| Average torque | Q |
| Synchronous inductance $L_{\rm d}$ | M,Q |
| Synchronous inductance $L_{\rm q}$ | Q |
| Open-circuit EMF | Q |

TABLE III
FINITE-ELEMENT SOLUTIONS REQUIRED WHEN THE $i-\psi$ LOOP IS IRREGULAR

| | |
|---|---|
| All performance parameters | *a, b, c, d...* |

However, from Fig. 3, $\alpha - \gamma = \pi/2 - \beta$, so

$$T = mp\frac{\psi_{\rm pk}i_{\rm pk}}{2}\cos\left(\frac{\pi}{2}-\beta\right) = mp\frac{\psi_{\rm pk}i_{\rm pk}}{2}\sin\beta. \tag{17}$$

If $\psi_{\rm pk}\sin\beta$ is now substituted from (10), we get

$$T = \frac{mp}{2}i_{\rm pk}\psi_{\rm Q}. \tag{18}$$

Equation (18) shows that the average electromagnetic torque can be computed from a single finite-element computation in which $\psi_{\rm Q}$ is computed. It also shows that $\psi_{\rm Q}$ is a direct measure of the torque per ampere. If $\gamma = 0$ and the current is in the $q$-axis, $I_d = 0$ and $L_d I_d = 0$, and the phasor diagram then shows that if the magnetic circuit is linear, point Q is independent of the current, and the torque per ampere is also constant. However, if $I_q$ is sufficient to saturate the magnetic circuit, point Q moves downward, and the torque per ampere decreases. This is often termed "kT roll-off", with kT being the torque per ampere. If $\gamma$ is nonzero, the effect of saturation is more complicated because, although (18) remains valid, $\psi_{\rm Q}$ varies in a more complex manner as a function of both the current and the phase angle $\gamma$.

The basic set of finite-element solutions required in the "GoFER" is summarized in Table II, the points being those denoted in Fig. 3.

### *E. Drives With Irregular $i-\Psi$ Loops: Time-Averaged $L_d$ and $L_q$*

Fig. 16 shows the $i-\Psi$ loop of a highly saturated three-phase IPM motor with six-step drive [1]. Because of the irregular shape of the loop, it is clear that many finite-element computations may be needed to get an accurate value for the area $W$ and the electromagnetic torque. In that case, the GoFER can be specified for all requirements as in Table III. A loop that is as irregular in shape as the one for a six-step drive can arise even when the windings are sine distributed. The shape is irregular because both the current and terminal voltage have nonsinusoidal time waveforms. However, nonsinusoidal time waveforms are perfectly admissible in $dq$ theory, and if the motor windings are sine-distributed $\Psi_{Md1}$, $L_d$ and $L_q$ will remain independent of rotor position even under saturated conditions. This implies that, even in a loop that is as irregular as Fig. 16, there are constant values of $\Psi_{Md1}$, $L_d$, and $L_q$

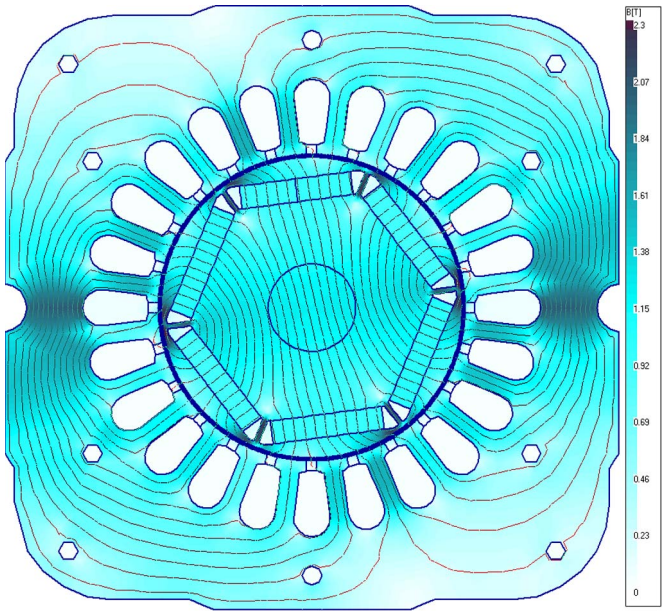


Fig. 4. Cross section with flux lines under load for the tested IPM motor.

that could be used to characterize the machine at this operating point.

In (5), we have a means of extracting the values of $\Psi_{Md1}$, $L_d$, and $L_q$ at any operating point—any rotor position—computed by the finite-element method. If we do this at a series of points $a, b, c, d \ldots$ around the $i-\psi$ loop, we can calculate average values for $\Psi_{Md1}$, $L_d$, and $L_q$ over one cycle. These average values can be combined in (4) with the time-averaged values of $i_d$ and $i_q$ to produce the time-averaged values of $\psi_d$ and $\psi_q$, from which the torque can be computed using (14).

If the $i-\psi$ loop is computed again with the time-averaged values and phasor values of the currents $I_d = i_d/\sqrt{2}$ and $I_q = i_q/\sqrt{2}$, it will be an ellipse with the same area $W$ as the actual loop. This suggests that the torque in an operating condition such as that of nonsinusoidal current can be computed using the phasor values of the (fundamental components of) voltage, current, and flux linkage, provided that the correct saturated values of $\Psi_{Md1}$, $L_d$, and $L_q$ are used. These values correspond to certain values of $i_d$ and $i_q$ (or $I_d$ and $I_q$), which means that lookup tables can be used in a torque estimator implemented in a control scheme. Numerical and experimental tests of this hypothesis are presented in the following section.

It should be observed that computing the $i-\psi$ loop with a reduced number of finite-element field evaluations does nothing to improve the estimation of iron loss, which depends on detailed flux-density waveforms at a large number of sites in the cross section and therefore seems to require a very much larger diet of finite-element analysis.

## III. Test and Computation Results

The numerical and experimental validation of the theoretical aspects from Section II is performed on a two-pole brushless IPM motor (Figs. 4–6). Each magnet pole comprises three separate NdFeB magnets. The three-phase winding is wye connected and approximately sine distributed. There is no skew. The finite-element flux plot shows a complex pattern of saturation. The noncircular shape of the stator causes imbalance between the phase flux linkages even for identical phase currents. However, this does not invalidate the use of the $i-\psi$ diagram, provided that all three phases are treated separately.

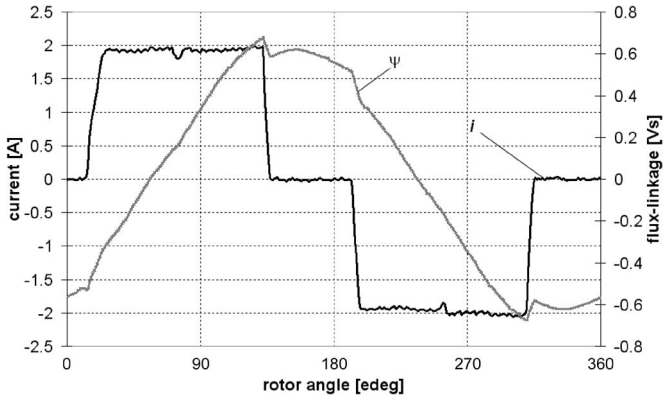


Fig. 5. Experimental current and flux-linkage waveforms for squarewave drive.

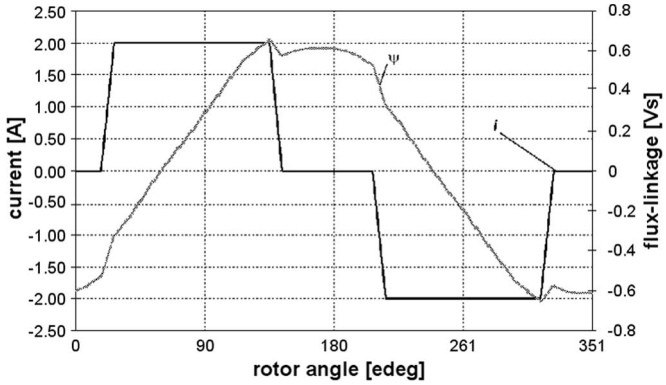


Fig. 6. Calculated current and flux-linkage waveforms for squarewave drive.

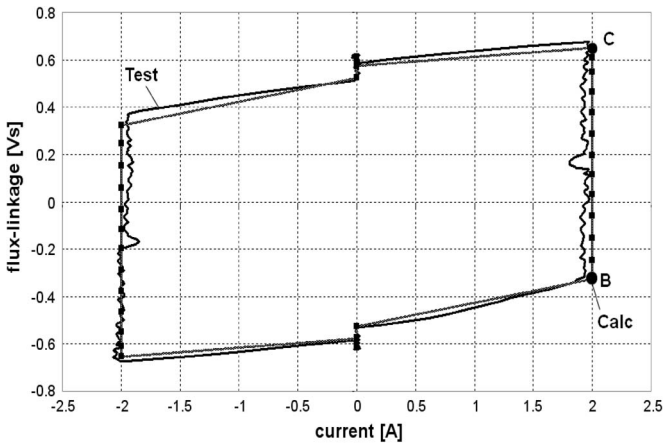


Fig. 7. Experimental and computed $i-\psi$ loop diagrams for squarewave drive.

### A. Squarewave Drive

The first analyzed case is when the test motor is controlled through a squarewave drive at 340 r/min, with 2-A peak current. Fig. 7 shows the superimposed measured and calculated $i-\psi$

TABLE IV
TORQUE VALUES FOR SQUAREWAVE DRIVE

| Method | Torque [Nm] |
|---|---|
| Torque transducer | 2.01 |
| Measured *i*-ψ loop | 2.00 |
| Calculated *i*-ψ loop | 1.95 |
| Calculated using only two points (B,C) (see Table 1) | 2.02 |

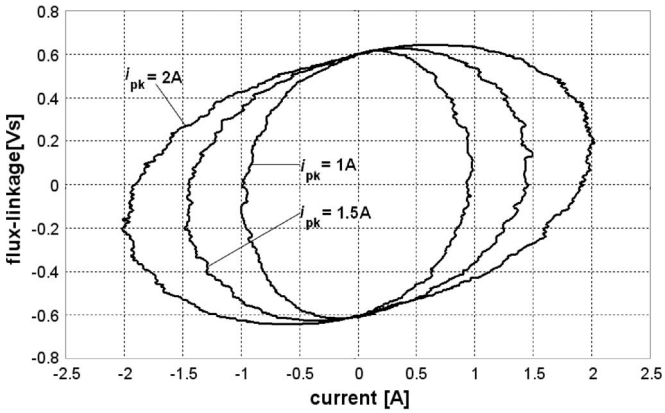


Fig. 8. Experimental $i-\psi$ loops for sinewave drive (current varies and $\gamma = 0$).

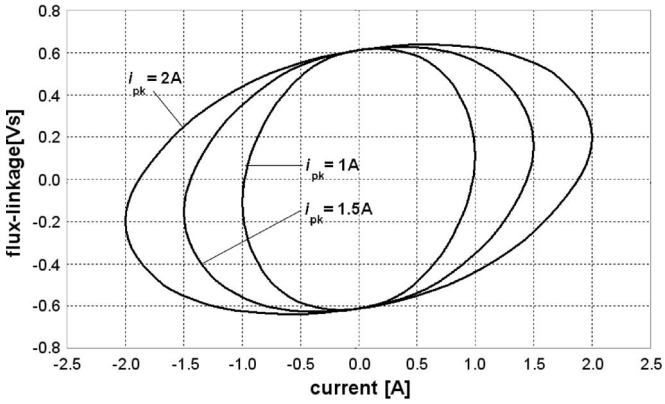


Fig. 9. Calculated $i-\psi$ loops for sinewave drive (peak current varies and $\gamma = 0$).

loops for squarewave drive. Table IV shows the measured and calculated torques. Note, in particular, the accurate result obtained with two-point finite-element calculation. Of course, this is possible only with an $i-\psi$ loop of such a regular shape.

### B. Sinewave Drive

Test and computed data are shown for the sinewave drive in Figs. 8–11. All the results for this configuration are obtained at 400 r/min. Tables V and VI show the comparison between measured and calculated torque values for different methods. As the analyzed motor saturates at a low current level, the intersection point Q of each $i-\psi$ loop with the flux-linkage axis does not change its position when the control angle $\gamma$ is kept constant (see Figs. 8 and 9).

When $\gamma$ varies, and the current is constant, point Q changes its position and reflects the variation of the average electromagnetic torque in accordance with (18) (see Figs. 10 and 11). The location of the points M and Q on the $i-\psi$ loops is further used to estimate $L_d$ and $L_q$ using (5).

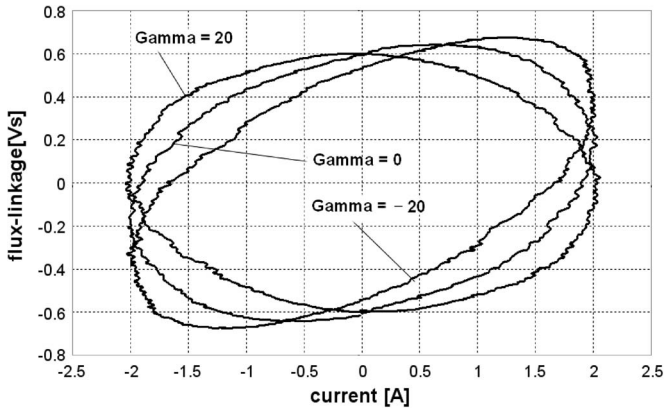


Fig. 10. Experimental $i-\psi$ loops for sinewave drive ($\gamma$ varies and constant peak current).

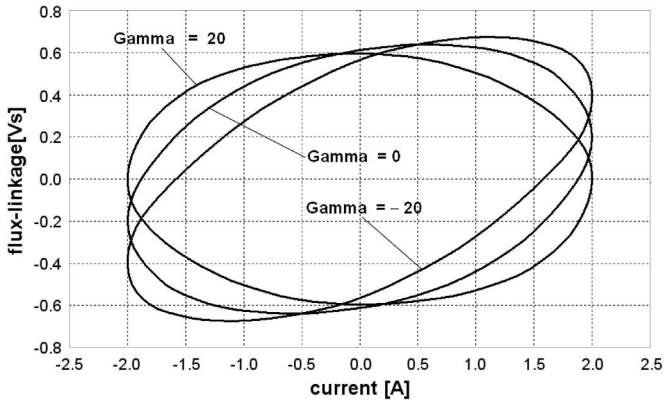


Fig. 11. Calculated $i-\psi$ loops for sinewave drive ($\gamma$ varies and constant peak current).

TABLE V
TORQUE VALUES FOR SINEWAVE-DRIVE, CONSTANT $\gamma = 0$ VARIABLE CURRENT

| Current [A] | Torque value [Nm] | | |
|---|---|---|---|
| | Test | Calc. i-ψ loops | Calc. 1 point (Q) |
| 1 | 0.86 | 0.89 | 0.90 |
| 1.5 | 1.32 | 1.33 | 1.35 |
| 2 | 1.81 | 1.78 | 1.79 |

TABLE VI
TORQUE VALUES FOR SINEWAVE-DRIVE, CONSTANT $I = 2$ A VARIABLE $\gamma$

| Gamma [edeg] | Torque value [Nm] | | |
|---|---|---|---|
| | Test | Calc. i-psi loops | Calc. 1 point (Q) |
| – 20 | 1.63 | 1.59 | 1.64 |
| 0 | 1.81 | 1.78 | 1.79 |
| 20 | 1.76 | 1.73 | 1.75 |

Fig. 12 shows the computed results for $L_d$ and $L_q$ as compared to the static measurement obtained with Jones' bridge [6], [8]. Fig. 13 shows the estimated back EMF under load from the flux linkage $\psi_{\mathrm{Q}}$ as a function of $I_q$.

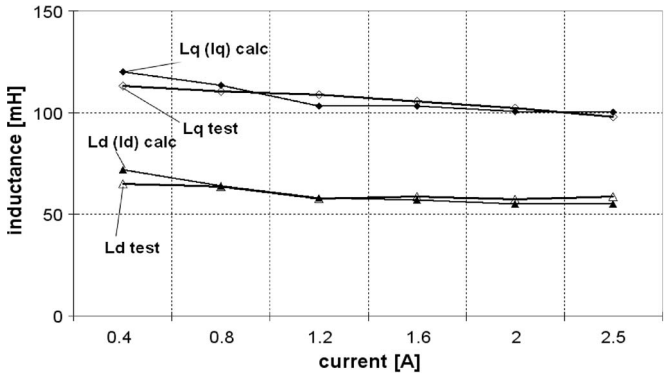


Fig. 12. Measured and computed inductances in the $d$–$q$ axis.

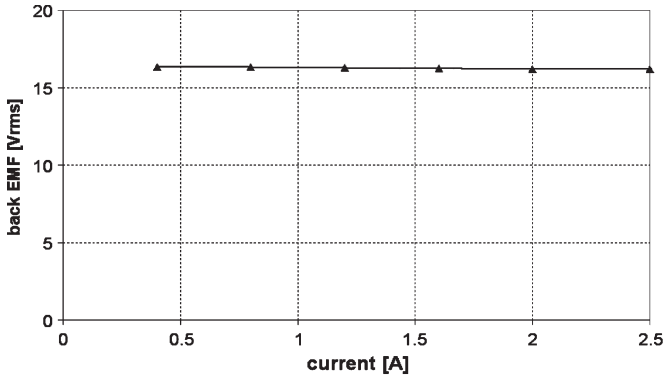


Fig. 13. Estimated back EMF under load conditions.

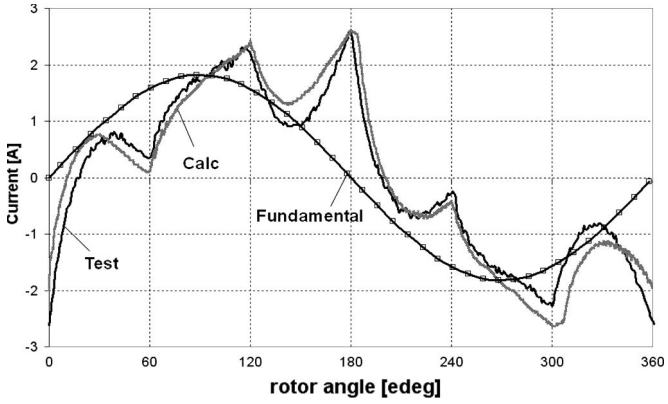


Fig. 14. Experimental and calculated current waveforms for six-step drive.

### C. Six-Step Drive

The case of the six-step drive provides a good example of an irregular current waveform. Tests are performed at a speed of 540 r/min and 80-V dc-link voltage. Figs. 14–16 show the experimental and computed waveforms. Table VII gives the torque values for different methods, including the usage of the current fundamental harmonic (amplitude and phase angle).

Because this motor has approximately sine-distributed windings, the torque calculated by (14) agrees closely with the test value, provided that "saturated" values are used for $L_d$, $L_q$, and $\Psi_{Md1}$.

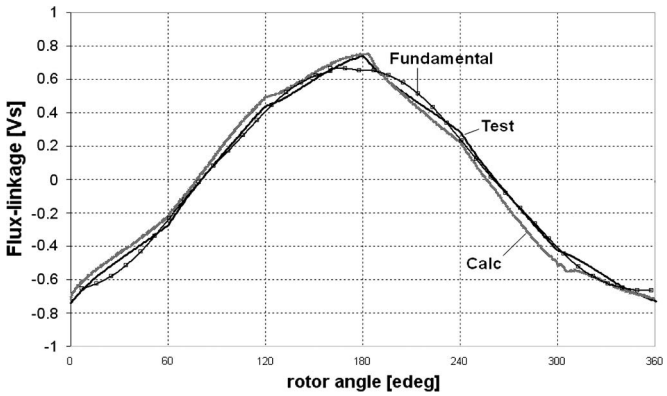


Fig. 15. Experimental and calculated flux-linkage waveforms for six-step drive.

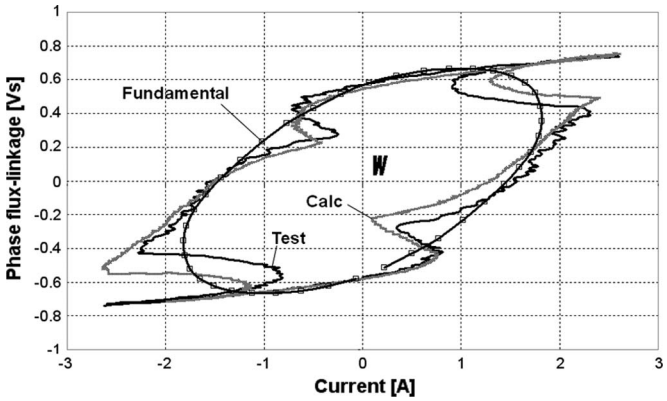


Fig. 16. Experimental and calculated $i-\psi$ loops for six-step drive.

TABLE VII
TORQUE VALUES FOR SIX-STEP DRIVE

| Method | Torque [Nm] |
|---|---|
| Torque transducer | 1.42 |
| Measured *i*-ψ loop | 1.42 |
| Calculated *i*-ψ loop | 1.45 |
| Calculated using the fundamental harmonic current and the averaged saturated $L_d$ and $L_q$ | 1.46 |

## IV. CONCLUSION

The flux–MMF diagram or "$i-\psi$ loop" is used to interpret several key features of the performance of brushless PM machines operating with both squarewave and sinewave drives. It is shown that important economies can be made in the application of the finite-element method to the accurate calculation of the average electromagnetic torque. This paper develops an improved understanding of the extent to which classical analysis and phasors can be used legitimately in extreme operating conditions such as six-stepping. In view of the deductions which can be made from the $i-\psi$ loop, it is surprising that it is not more widely used. By means of simple geometric deductions, it bypasses (or at least illustrates) the complex mathematics of the $dq$ transformation. It also provides a means of testing the rigor of various common assumptions about the motor—for example, whether the synchronous inductances vary with rotor position or whether the phasor diagram can be used when the current waveform is not sinusoidal. The graphical presentation

of the $i-\psi$ loop complements and illustrates a number of the recent works on saturated brushless machines (particularly the IPM motor) by several different authors and for several different applications.

## ACKNOWLEDGMENT

The authors would like to thank P. Scavenius, N. C. Weihrauch, and P. E. Hansen of Danfoss Compressors, Flensburg, Germany, who supplied the special test motor used in this paper. The authors would also like to thank the support of the member companies of the SPEED Consortium and the assistance of P. Miller and I. Young of the SPEED Laboratory.

## REFERENCES

[1] T. J. E. Miller, M. Popescu, C. Cossar, and M. I. McGilp, "Computation of the voltage-driven flux–MMF diagram for saturated PM brushless motors," in *Conf. Rec. IEEE IAS Annu. Meeting*, Hong Kong, Oct. 2004, vol. 2, pp. 1023–1028.

[2] D. M. Ionel *et al.*, "Assessment of torque components in brushless permanent-magnet machines through numerical analysis of the electromagnetic field," *IEEE Trans. Ind. Appl.*, vol. 41, no. 5, pp. 1149–1158, Oct. 2005.

[3] M. A. Jabbar, L. Zhejie, and D. Jing, "Time-stepping finite-element analysis for the dynamic performance of a permanent magnet synchronous motor," *IEEE Trans. Magn.*, vol. 39, no. 5, pp. 2621–2623, Sep. 2003.

[4] B. Štumberger *et al.*, "Evaluation of saturation and cross-magnetization effects in interior permanent-magnet synchronous motor," *IEEE Trans. Ind. Appl.*, vol. 39, no. 5, pp. 1264–1271, Sep./Oct. 2003.

[5] N. Bianchi and S. Bolognani, "Magnetic models of saturated interior permanent magnet motors based on finite element analysis," in *Conf. Rec. IEEE IAS Annu. Meeting*, St. Louis, MO, 1998, pp. 27–34.

[6] T. J. E. Miller, *SPEED's Electric Motors*.

[7] T. M. Jahns, G. B. Kliman, and T. W. Neumann, "Interior permanent-magnet synchronous motors for adjustable-speed drives," *IEEE Trans. Ind. Appl.*, vol. IA-22, no. 4, pp. 738–747, Jul. 1986.

[8] T. J. E. Miller, "Methods for testing permanent-magnet AC motors," in *Conf. Rec. IEEE IAS Annu. Meeting*, Toronto, ON, Canada, Oct. 1981, pp. 494–499.

[9] D. A. Staton, W. L. Soong, R. P. Deodhar, and T. J. E. Miller, "Torque prediction using the flux–MMF diagram in AC, DC and reluctance motors," *IEEE Trans. Ind. Appl.*, vol. 32, no. 1, pp. 180–188, Jan./Feb. 1996.

[10] M. A. Jabbar, L. Zhejie, and D. Jing, "Time-stepping finite-element analysis for the dynamic performance of a permanent magnet synchronous motor," *IEEE Trans. Magn.*, vol. 39, no. 5, pp. 2621–2623, Sep. 2003.

**T. J. E. Miller** (M'74–SM'82–F'96) is a native of Wigan, U.K. He received the B.Sc. degree from the University of Glasgow, Glasgow, U.K., and the Ph.D. degree from the University of Leeds, Leeds, U.K.

He is a Professor of electrical power engineering and the Founder and Director of the SPEED Consortium, University of Glasgow, where he is currently with the SPEED Laboratory, Department of Electronics and Electrical Engineering. He is the author of over 100 publications in the fields of motors, drives, power systems, and power electronics, including seven books. From 1979 to 1986, he was an Electrical Engineer and Program Manager with GE Research and Development, Schenectady, NY, and his industrial experience includes periods with GEC (U.K.), British Gas, International Research and Development, and a student apprenticeship with Tube Investments Ltd.

Prof. Miller is a Fellow of the Institution of Electrical Engineers, U.K.

**Mircea Popescu** (S'98–M'98–SM'04) was born in Bucharest, Romania. He received the M.Eng. and Ph.D. degrees in electrical engineering from the University "Politehnica" of Bucharest, Bucharest, Romania, in 1984 and 1999, respectively, and the D.Sc. degree in electrical engineering from Helsinki University of Technology, Espoo, Finland, in 2004.

He has over 20 years of experience in industrial research and development as a Project Manager with the Research Institute for Electrical Machines (ICPE-ME), Bucharest, and as a Research Scientist with the Electromechanics Laboratory, Helsinki University of Technology. Since 2000, he has been with the SPEED Laboratory, Department of Electronics and Electrical Engineering, University of Glasgow, Glasgow, U.K., as a Research Associate Fellow. His main research interests include modeling and optimization of ac machines and drives.

**Calum Cossar** was born in Hamilton, U.K., in 1962. He received the B.Sc.(Hons.) degree in electronics and electrical engineering from the University of Glasgow, Glasgow, U.K., in 1983.

From 1983 to 1988, he was with Ferranti plc, Edinburgh, U.K., where he worked on the design of high-speed digital signal processing for airborne radar applications. Since 1988, he has been with the SPEED Laboratory, Department of Electronics and Electrical Engineering, University of Glasgow, as a Research Assistant. He became a Research Technologist and has been involved in research and development into the implementation of switched reluctance control.

**Malcolm I. McGilp** was born in Helensburgh, Scotland, in 1965. He received the B.Eng.(Hons.) degree in electronic systems and microcomputer engineering from the University of Glasgow, Glasgow, U.K., in 1987.

Since graduation, he has been working with the SPEED Laboratory, Department of Electronics and Electrical Engineering, University of Glasgow, first as a Research Assistant from 1987 to 1996 and as a Research Associate since then. He is responsible for the software architecture of the SPEED motor design software and has developed the interface and user facilities which allow it to be easy to learn and integrate with other PC-based software.

**Mircea Olaru** received the M.Sc. degree in mathematics from the University of Bucharest, Bucharest, Romania.

He is currently an Analyst and Programmer with ICNDMF-CEFIN, Bucharest, Romania. He has more than 35 years of experience in finite-element analysis in electromagnetics and mechanics. He has authored 35 published articles and has presented 54 essays at national and international scientific meetings.

**Alan Davies** received the B.Sc. degree (with first class honors) in computing science from Staffordshire University, Stoke on Trent, U.K., in 1984.

He was with the Electromagnetics Group, GEC Engineering Research Centre, to assist in the development of the company's finite-element methods in electromagnetic analysis. Since then, he has been responsible for much of the development of the commercial code "SLIM Electromagnetic Engineering" which is currently in its third major revision. He is currently with the AREVA T&D Technology Centre, Stafford, U.K. His special interests include computer graphics and geometric modeling.

**Jonathan Sturgess** was born in Knutsford, U.K., in 1959. He received the M.S. degree in engineering science, economics, and management from the University of Oxford, Oxford, U.K., in 1981, and the Ph.D. degree from Imperial College, London, U.K., in 1987, with a dissertation entitled "Finite Element Electromagnetic Analysis of Generator Transient Performance."

He was with British Rail Engineering Ltd. (BREL) before he pursued his Ph.D. studies. Since completing the Ph.D. degree, he has been with the AREVA T&D Technology Centre, Stafford, U.K. His principal occupation is the modeling of electromagnetic fields in power engineering apparatus and developing the tools and techniques contained in the SLIM Electromagnetic Engineering package. His particular interest includes time-varying field simulation using the finite-element method.

Dr. Sturgess is a Chartered Engineer in the U.K. and a member of the Institution of Engineering and Technology.

**Alessandra Sitzia** (M'91) was born in Cagliari, Sardinia, in 1961. She received the B.S. degree in electrical and electronic engineering in 1982 and the Ph.D. degree in 1985 from the University of Leeds, Leeds, U.K., with a dissertation entitled "Torque in Elementary Variable Reluctance Machines."

She spent eight years at the University of Manchester Institute of Science and Technology (currently the University of Manchester), Manchester, U.K., as a Postdoctoral Researcher and then a Lecturer, specializing in electromagnetic analysis of electrical machines. Since 1993, she has been with the AREVA T&D Technology Centre, Stafford, U.K. She is particularly involved in the electromagnetic analysis of power transformers and in developing the SLIM Electromagnetic Engineering software.

Dr. Sitzia is a member of the Institution of Engineering and Technology.